Environmental Science and Pollution Research (2024) 31:38908–38925
https://doi.org/10.1007/s11356-023-26884-8

CLEANER PRODUCTION AND SUSTAINABLE PROCESSES FOR ENVIRONMENTAL REMEDIATION

Mitigating environmental impact by development of ambient-cured EAF slag and fly ash blended geopolymer via mix design optimization

Anant Mishra[1] · **Mukund Lahoti**[1] · **En-Hua Yang**[2]

Received: 20 December 2022 / Accepted: 4 April 2023 / Published online: 27 April 2023

Abstract

This article discusses the utilization of industrial by-products, namely, electric arc furnace slag (EAFS) and fly ash to produce cementless geopolymer binder. Taguchi-grey optimization is used for experimental design and for investigating the effects of mix design parameters. Fly ash, in the levels of 0–75% (by mass), partly replaced EAFS in the binary-blended composite system. Experiments were performed on the microstructural development, mechanical properties, and durability of ambient-cured EAFS-fly ash geopolymer paste (EFGP). The optimal mix with 75–25% composition of EAFS and fly ash produced ~ 39 MPa compressive strength accrediting to the co-existence of C-A-S–H and N-A-S–H gels. The initial and final setting times were 127 min and 581 min, respectively, owing to adequate alkali and amorphous contents in the matrix, and the flowability was 108% due to sufficient activator content and the spherical shape of fly ash particles. SEM, XRD, and FTIR results corroborated the mechanical test results.

Keywords Electric arc furnace slag · Fly ash · Geopolymer · Ambient-cured · Taguchi-grey relational analysis · Optimization

Abbreviations

EAFS	Electric arc furnace slag
EFGP	Electric arc furnace slag-fly ash geopolymer paste
SEM	Scanning electron microscopy
XRD	X-ray diffraction
FTIR	Fourier transform infrared spectroscopy
OPC	Ordinary portland cement
GRA	Grey relational analysis
A/B ratio	Alkaline solution to binder ratio
SH(M)	Sodium hydroxide (molarity)
SS/SH ratio	Sodium silicate to sodium hydroxide ratio
DOE	Design of experiments
f'cu	Compressive strength
GRG	Grey relational grade
S/N ratio	Signal to noise ratio
(S/N)mean	Mean of signal to noise ratio

Responsible Editor: Philippe Garrigues

✉ Mukund Lahoti
mukund.lahoti@pilani.bits-pilani.ac.in

[1] Department of Civil Engineering, Birla Institute of Technology and Science, Pilani, Pilani 333031, India

[2] School of Civil and Environmental Engineering, Nanyang Technological University, Singapore 639798, Singapore

Introduction

The demand for steel is increasing every successive year. According to the short-range outlook published by the World Steel Association (2021), nearly a growth rate of around 2.2%, i.e., 1896.4 million tons (Mt) in steel demand, is expected for 2022. The production of crude steel dominantly involves two routes, namely, the integrated route, which incorporates basic oxygen furnace (BOF) /blast furnace (BF) plants, and the electro-steel route which is also known as the electric arc furnace (EAF) route (Nguyen et al. 2022). The primary distinction between the former and latter is the raw material. The integrated route feeds iron ore, ferrous scraps up to 30%, coal, and limestone, and the EAF feeds recycled steel, sponge iron and limestone (World Steel Association 2011), (Rahou et al. 2022). The major challenge associated with steel production is its energy-intensive process and CO_2 emissions (Aayog and Action 2018). The EAF route is much more sustainable than the integrated path, with 63% less carbon emissions and 57%, 87%, and 67.5% less consumption

of iron ore, coal, and limestone, respectively (World Steel Association 2011), (Steel and Report 2019). Due to the low CO_2 emissions and energy requirements, the EAF route is mandatory for crude steel production worldwide as it was projected that by shifting 53% of steel production to the EAF route, net-zero emissions could be achieved (IEA 2021). EAF slag (EAFS) is an industrial waste generated while melting scrap steel, accounting for roughly 15–20% of total steel quantity (Li et al. 2022), (Han et al. 2015). It largely gets accumulated in landfills causing environmental hazards due to the heavy metals leachates (Singh et al. 2021). Utilization of this waste concerns most developed and developing nations, with the primary focus being to complete the life cycle of the products (Shrivas et al. 2022).

With this frame of reference, previous literature (Pellegrino and Gaddo 2009) has reported the potential use of EAFS in conventional cement concrete by replacing natural aggregates with EAFS aggregates due to its low crushing value and rough texture which provides better interlocking. Additionally (Singh et al. 2021), investigated the leaching behavior of EAFS and recommended its usage as a sustainable building material due to negligible or permissible leachates. Yet, very limited studies have focused on the use of EAFS as a binder.

In this context, a novel material, namely, geopolymer, can effectively rectify the problem of waste accumulation. Geopolymers are eco-friendly green construction materials produced by alkali activation of alumino-silicate precursor/s to achieve binding properties similar to ordinary Portland cement (OPC) (Davidovits 1989; Duxson et al. 2007; Lahoti et al. 2019; Nemaleu et al. 2022). The manufacturing of OPC consumes extensive energy, i.e., around 12–15% of the entire share across the globe (Thwe et al. 2021), and is also accountable for greenhouse gas emissions (Salas et al. 2016). This indicates the need for a competent binder to achieve our sustainable development goals, without compromising with the performance as obtained using OPC. Literature report that similar performance could be achieved using geopolymer cement with lower carbon emissions as compared to OPC (Bajpai et al. 2020; Meshram and Kumar 2022). A comprehensive LCA using cradle-to-gate approach was performed in these studies. Moreover, geopolymers significantly reduce carbon footprints (McLellan et al. 2011) along with employing industrial wastes such as fly ash, blast furnace slag, and silica fume to produce value-added products (Assi et al. 2020).

Despite being a sustainable and energy-efficient cementless binder, the in-situ application of geopolymers, in general, gets limited by the need of heat curing. Table 1 highlights that EAFS is a potential precursor for geopolymers; however, the majority of literature (as shown in Table 1) has focused on heat curing to achieve higher performance (Češnovar et al. 2019; Ozturk et al. 2019). However, high performance is not solely dependent on the curing temperature but is also affected by the precursor content, activator dosage, and activator concentration (Shilar et al. 2022). Thus, mix-design tailoring at ambient curing conditions is essential. It will be advantageous if optimum compressive strength, flowability, and setting time could be achieved without the high-temperature curing (i.e., at room temperature) through optimization of mix design parameters. Besides, in this study, fly ash is used as a modifier to replace EAFS proportionately. It has been observed that high calcium content in EAFS causes drying shrinkage, low flowability, and reduced setting times. Partly replacing EAFS with fly ash can improve the fresh and hardened geopolymer properties (Rashad et al. 2021).

It is evident from the literature that several parameters may impact the attributes of EFGP. A substantial number of trials are needed to optimize the parameters. However, this process will consume a lot of time and money. The number of experiments can be significantly reduced by selecting an efficient design of the experiment approach (Hadi et al. 2017; Suji et al. 2021; Rawat et al. 2022). Taguchi design is the most effective and adaptive technique used for optimizing process parameters, and it entails testing a set of experimental parameters that are expected to create a variance in output parameters across a wide variety of experimental setups. These are also useful for showing the best result for a given set of input parameters. Furthermore, the grey relational analysis (GRA) technique can be used to create a specialized set of optimal levels for several attributes (responses) at the same time.

As briefly reviewed above, there have been previous studies, prominently on the production of heat-cured EAFS-based geopolymer, whereas ambient-cured geopolymers are still in the research phase. The synergetic study of the parameters on the fresh properties like flowability and setting time of ambient cured EFGP are too scant. Therefore, there is a need to investigate the combined effect of parameters such as EAFS replacement level (percent by mass of total binder), A/B ratio, SH molarity, and SS/SH ratio on the properties of ambient cured EFGP. To the best of our knowledge, no prior study in literature has utilized Taguchi design or Taguchi-GRA to develop ambient cured EFGP. Thus, the objective of this study is to conduct a design of experiments (DOE) using the Taguchi method and GRA to investigate the combined effect of mix parameters on ambient cured EFGP properties (setting times, flowability, and compressive strength). Furthermore, a verification experiment is conducted, and durability and microstructural investigation is performed on the optimum mixes.

Experimental program

Material

EAFS and fly ash were the aluminosilicate precursors used to develop the geopolymer. EAFS was procured from

Table 1 Mix design and observations by researchers for developing EAFS geopolymer

Precursor	Mix design parameters					Observation*			Ref
	EAFS (%)	A/B	SH (M)	SS/SH	Curing temp. (℃)	Highest f'_{cu} (MPa)	Flowability (%)	Optimum Mix	
EAFS C&D waste Red mud	0–50	0.27 to 0.3	8,10, 12	N.R	80	~75	N.R	EAFS-100% SH -10 M	(Zaharaki et al. 2016)
EAFS	100	0.13	4, 6, 8	1,1.5, 2	40, 80	~22	N.R	SH-6 M Temp-80 ℃	(Ozturk et al. 2019)
EAFS and Fly ash	0–100	0.28 to 0.35	8	N.R	85	~28	N.R	EAFS-50%	(Cristelo et al. 2019)
EAFS Fly ash	0–40	0.77	10	N.R	65	~33	N.R	EAFS-30%	(Niklioć et al. 2016)
EAFS Metakaolin	20–40	0.25	8	N.R	R.T	– 50	30–50	EAFS-80%	(Bignozzi et al. 2010)
EAFS EAF dust	93–100	0.25	10	1.5	65	~21	N.R	EAFS-100%	(Nikolic et al. 2020)
EAFS, Fly ash, WFS	0–30	0.40	8	2.5	R.T	~26	N.R	EAFS-30%	(Apithanyasai et al. 2020)
EAFS, GGBS, cement kiln dust	10–75	0.34	N.R	N.R	40	– 25	N.R	EAFS-50%	(Khater 2015)
EAFS, TMW	20–50	0.25	10	2	60	– 30	N.R	EAFS-50%	(Sedira and Castro-Gomes 2019)
EAFS, Ladle slag	0–100	0.5	N.R	N.R	R.T, 50, 70, 90	~57	N.R	EAFS-50% Temp-R.T	(Češnovar et al. 2019)
EAFS, Fly ash	15–60%	0.3	10	3	40	– 75	60–104	EAFS-70%	(Rashad et al. 2021)

1. *A/b* alkaline solution (sodium silicate solution + sodium hydroxide solution) to the binder ratio, *SH(M)* sodium hydroxide (molarity), *SS/SH* sodium silicate to sodium hydroxide ratio

2. *N.R* not reported, *R.T* room temperature, *WFS* waste foundry sand, *TMW* Tungsten mine waste

*Observations pertaining to setting time is not reported in literature

Valley Iron Steel Company Limited, Ponta Sahib, Himanchal Pradesh, India. Fly ash (class F) conforming to ASTM C618-17 (ASTM C 618 2014) was brought from the ROSA power plant, in Shahjahanpur, India. The comparison of particle size (d_{50}), specific gravity, and surface area of EAFS and fly ash and the chemical composition (observed using Malvern Panalytical Epsilon1 XRF spectrometer) is shown in Tables 2 and 3. Microstructure (observed using FE-SEM, Apreo LoVac) and mineralogical characteristics (observed using Rigaku Miniflex X-Ray diffractometer with CuK radiation ($\lambda = 1.5405$ Å) of EAFS and fly ash are shown in Figs. 1 and 2. Fly ash particles are spherical, whereas EAFS particles are angular and irregular in shape. While the XRD spectrum reveals amorphous content, including crystalline phases of quartz and mullite, EAFS primarily consists of crystalline phases, such as fly ash primarily as calcite, hematite, gehlenite, and quartz. For the activation of precursor, NaOH pellets with a purity of 98.8% and Na_2SiO_3 solution with composition ($Na_2O = 15.50\%$, $SiO_2 = 31\%$, $H_2O = 53.5\%$, specific gravity = 1.56, Baume = 51, and weight ratio = 2.0) was used.

Table 2 Properties of EAFS and fly ash

	Particle size (d_{50}) (mm)	Specific gravity (g/kg)	Surface area (m^2/kg)
EAFS	0.020	3.14	550
Fly ash	0.034	2.24	330

Methods

Parametric optimization of EFGP

Taguchi method developed by Genichi Taguchi (J 1987; Arslanoglu 2017) was initially used to optimize the factors including EAFS content, A/B ratio, SH molarity, and SS/

Table 3 Chemical composition of EAFS and fly ash

	SiO_2	Al_2O_3	CaO	Fe_2O_3	SO_3	K_2O	Cr_2O_3	TiO_2	MnO	LOI*
EAFS	29.48	5.45	49.49	7.40	0.94	4.14	0.63	1.16	0.749	0.64
Fly ash	54.70	26.62	2.48	8.69	0.18	2.05	0	3.47	0.06	2.20

*Loss of ignition

SH ratio, which are the most significant factors affecting EFGP properties. In this analysis, four levels were specified for each parameter as indicated in Table 4. The full factorial design approach requires 256 (i.e., $Level^{Parameters}$: 4^4) experimental trial combinations to fully assess the impact of each parameter, which is a resource-intensive process. However, the experiment was set up as an L16 orthogonal array with 16 different combinations of variables using the Taguchi method. Table 5 provides a list of the 16 geopolymer mixtures along with the corresponding initial setting time, final setting time, flowability, compressive strength (f'_{cu}), and water absorption. The data collected underwent statistical and graphical analysis using Minitab software (Version 19.1).

The signal-to-noise ratio (S/N) was then obtained using Eqs. 1 and 2 for initial setting time, final setting time, flowability, and f'_{cu} (Hadi et al. 2017).

$$(S/N)_{ij} = -10 \times \log_{10}\left[\frac{1}{n}\sum_{i=1}^{n}\frac{1}{Y_{ij}^2}\right] \Rightarrow {}^{\varepsilon}\text{Highest is the best}^{\varepsilon}\text{ function} \quad (1)$$

$$(S/N)_{ij} = -10 \times \log_{10}\left[\frac{1}{n}\sum_{i=1}^{n}Y_{ij}^2\right] \Rightarrow {}^{\varepsilon}\text{ Lowest is the best}^{\varepsilon}\text{ function} \quad (2)$$

where $\boldsymbol{Y_{ij}}$ stands for the experimental outcome of ith experimental trial for jth response in the nth replication.

The contribution percentages of each parameter attributed to initial setting time, final setting time, flowability, and f'_{cu} were quantified using analysis of variance (ANOVA) (Nazari and Sanjayan 2015).

Furthermore, grey relational analysis (GRA), which is a widely adopted technique was employed to reach a single combination of optimum level through processed parameters for the required attributes concurrently (Jamshaid et al. 2022). The grey relational grade, abbreviated $GRG(\mathcal{G})$, was calculated using Eq. 3 for each mix. The higher the relational grade of a parameter combination, the more likely it is to be optimal.

$$\mathbf{GRG}_i = \mathcal{G}_i = \frac{1}{n}\sum_{k=1}^{n} w_j \xi_i(k) \quad (3)$$

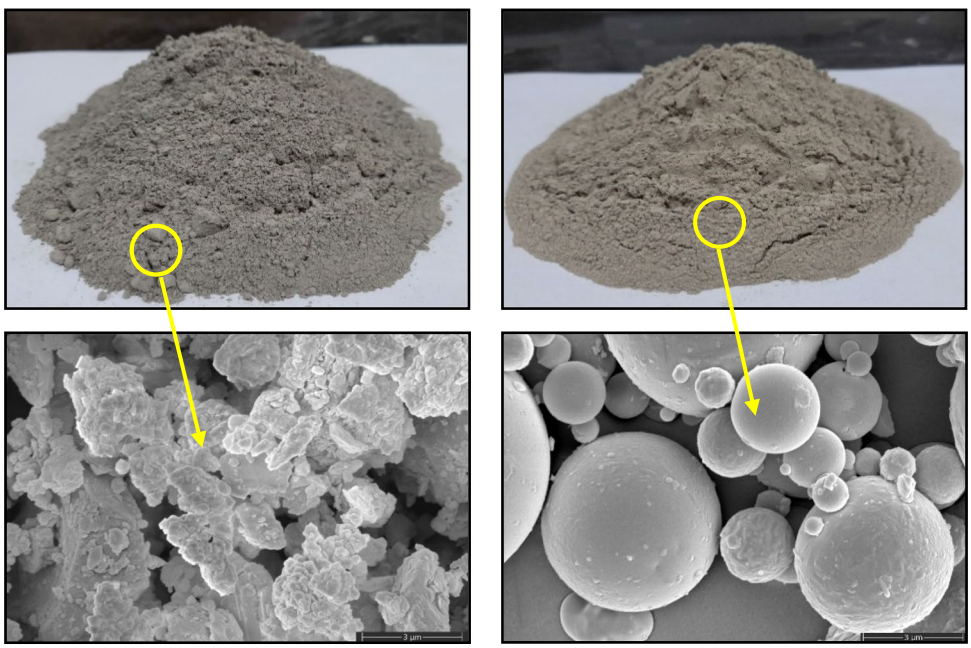

(a) (b)

Fig. 1 General and microscopic views of precursors **a** EAFS and **b** Fly ash

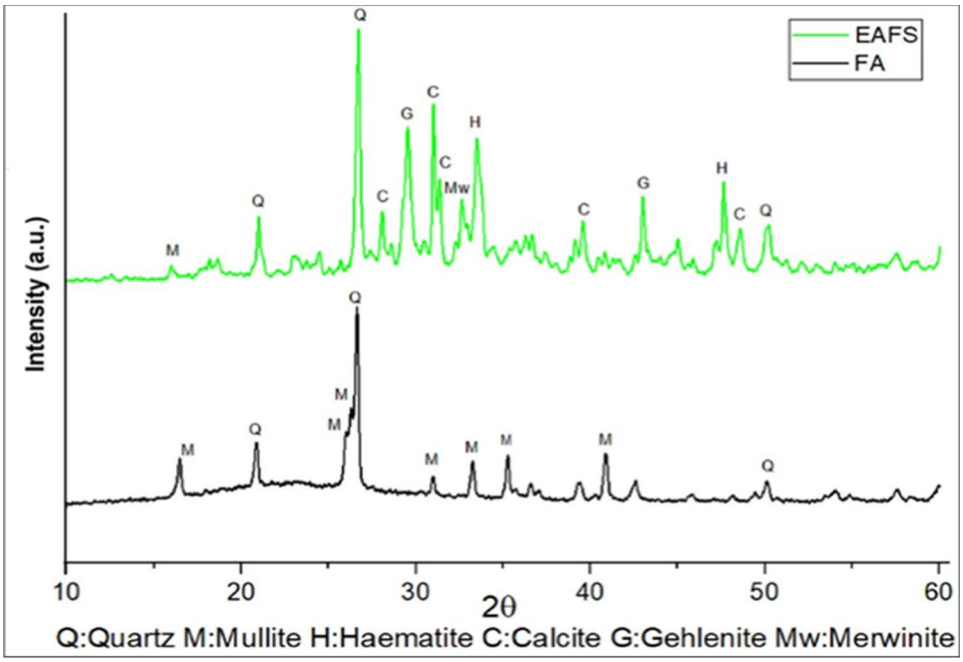

(a)

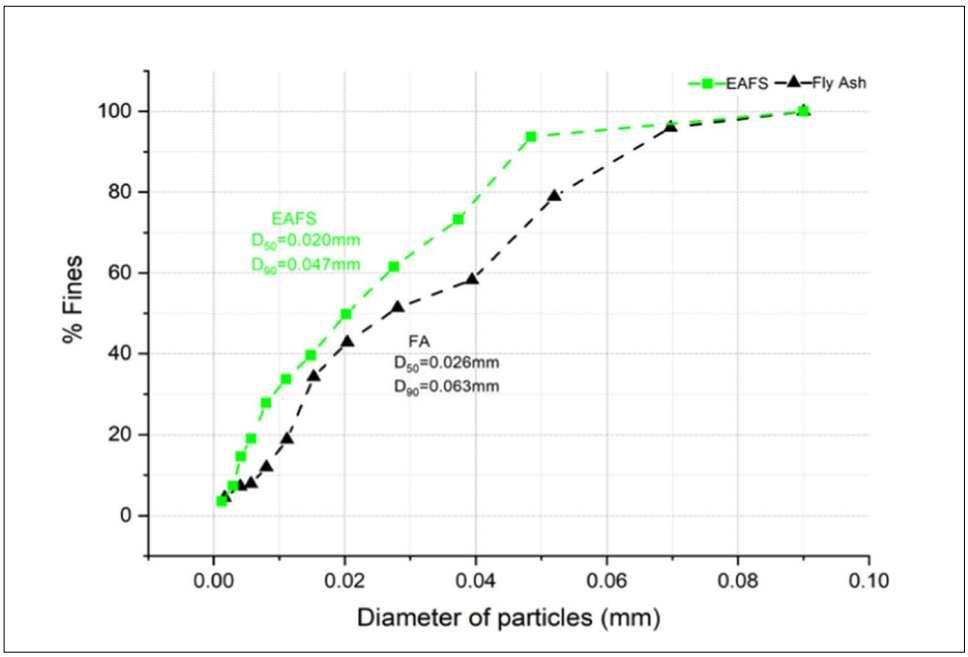

(b)

Fig. 2 **a** XRD patterns of EAFS and fly ash. **b** Particle size distribution

Table 4 Parameters and their corresponding levels

Parameters	Levels			
	1	2	3	4
EAFS	100	75	50	25
A/B	0.35	0.40	0.45	0.50
SH molarity	8	10	12	14
SS/SH	1.5	2.0	2.5	3.0

where *w* stands for the normalized weight assigned to the *j*th response of the *i*th experiment, where w is equal to 1 (Kuo et al. 2008; Narong et al. 2018).

Mixture preparation

To examine the consistency, compressive strength, and microstructural development of EFGP, sixteen different combinations of geopolymer paste with varying EAFS/fly

Table 5 L_{16} orthogonal array based on the Taguchi method and corresponding setting times, flowability, compressive strengths, and water absorption

Mix	EAFS	A/B	SH (M)	SS/SH	IST (min)	FST (min)	FV (%)	f'$_{cu}$ (MPa)	Water absorption (%)
M1	100	0.35	8	1.5	25	300	40	4.6 ± (0.3)	21.6
M2	100	0.4	10	2	38	345	55	12.8 ± (0.5)	19.3
M3	100	0.45	12	2.5	86	425	66	23.7 ± (1.2)	13.7
M4	100	0.5	14	3	50	410	70	21.1 ± (0.8)	13.9
M5	75	0.35	10	2.5	95	495	55	24.9 ± (1.3)	13.6
M6	75	0.4	8	3	105	540	70	21.1 ± (1.9)	13.9
M7	75	0.45	14	1.5	120	565	95	36.4 ± (2.7)	12.0
M8	75	0.5	12	2	130	620	110	34.9 ± (1.8)	12.2
M9	50	0.35	12	3	105	685	55	18.6 ± (1.6)	15.2
M10	50	0.4	14	2.5	110	715	94	29.4 ± (1.8)	12.3
M11	50	0.45	8	2	190	735	112	40.4 ± (2.3)	10.9
M12	50	0.5	10	1.5	200	760	128	17.5 ± (1.6)	18.6
M13	25	0.35	14	2	165	810	65	13.9 ± (1.1)	18.9
M14	25	0.4	12	1.5	210	835	95	19.5 ± (1.4)	14.4
M15	25	0.45	10	3	290	860	116	27.1 ± (1.9)	12.6
M16	25	0.5	8	2.5	320	910	135	10.3 ± (0.1)	19.5

IST initial setting time, *FST* final setting time, *FV* flowability

ash, A/B, SH molarity, and SS/SH ratios were cast using the Taguchi design of experiments method, as shown in Table 5.

Figure 3 depicts the formation of the EFGP. Firstly, SH flakes were poured into tap water to dissolve for obtaining the desired molarity (8–14 M) of solution before 24 h. Then SH solution was thoroughly mixed with sodium silicate solution to obtain the alkali activators and after that samples were prepared in three steps: (1) dry mixing of EAFS and fly ash for about 2 min in the mixer; (2) slow mixing of the activator solution in the dry powder for about 3 min to form a homogeneous slurry; (3) pouring the blended paste in molds and vibrating it for a minute and leveling the top surface. Samples were then packed in airtight plastic bags and kept at ambient temperature (27 ± 1.5 °C) for 24 h and then de-mold and stored in airtight containers (to resist moisture loss) at ambient temperature till further testing.

Experimental test

As per the ASTM C191-08 (ASTM C191 2013) and IS 4031 (IS: 4031 (Part 5) 2000), the initial and final setting time of the fresh geopolymer pastes were recorded using the Vicat's apparatus (see Fig. 4 a). For obtaining the initial setting, the time from pouring the paste in the mold to the time at which 25 mm pen penetration achieved by 1 mm diameter needle was noted, and for the final setting, the time at which no impression made on cake by 10 mm diameter needle was reported. According to ASTM C1437 (ASTM C1437-99 1999) (ASTM 2001) the flow table was used to measure the flow properties of the fresh paste (see Fig. 4 b).

According to ASTM C109/C109M-16a (ASTM C109 2008) the compressive strength test was conducted on all 16 mixes obtained from the L16 orthogonal array on an AIMIL

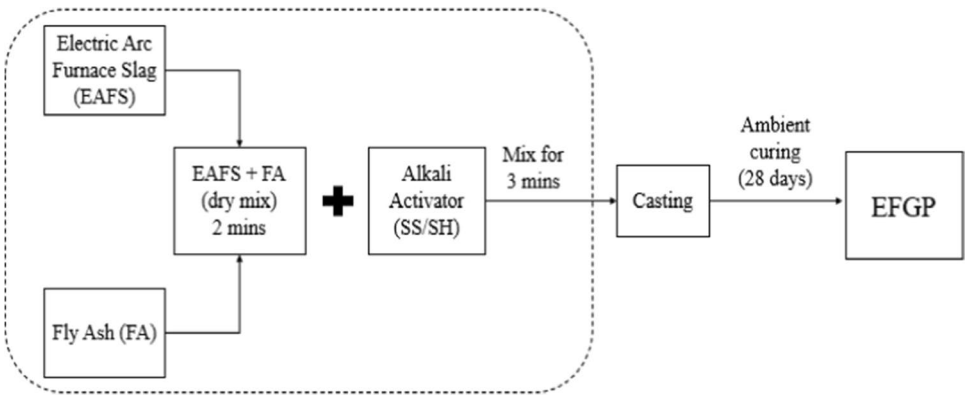

Fig. 3 Mixing sequence of ingredients of EFGP mix

(a) (b)

Fig. 4 Fresh properties test for EFGP. **a** Setting time. **b** Flowability

2000 kN compression testing machine at 28 days. The three samples (50 × 50 × 50 mm cubes) were tested and the average value f'$_{cu}$ has been reported.

Water absorption is a direct indicator of surface porosity (Rashad and Gharieb 2021) and high water absorption makes the matrix more sensitive to sulfate attack, chloride ion diffusion, and acid attack, etc., which has a substantial impact on the specimen's performance (Zhang and Zong 2014). Hence, the durability of EFGP samples was assessed by calculating the water absorption. The water absorption test was performed in accordance to ASTM C 140–01 (ASTM C140 2012). Fifty millimeter cubes were placed at 110 °C for 24 h in an oven to ensure zero moisture conditions, and dry weight, W_d was measured. After that, the cubes were immediately placed in a water tank for the next 24 h, and wet weigh, W_w was measured. Water absorption was then calculated by Eq. 4.

$$\text{Water Absorption } (\%) = \left(\frac{W_W - W_d}{W_d}\right) \times 100 \quad (4)$$

Microstructural study

The microstructural examination was conducted on fractured surfaces of the geopolymer mix from the selected tested specimens. XRD analysis was carried out using a Rigaku Smart lab 9 W model diffractometer with (λ = 1.504 Å) Cu Kα radiation in the 2θ range of 10° to 60° at a scan rate of 2°/min. XPert high score plus diffraction software was used to evaluate the data (PAN analytical) and origin software was employed to calculate the crystallinity of the samples by dividing the area of the crystalline phases by the cumulative area.

The functional groups of the precursors and the geopolymer samples were determined using FTIR analysis. For making sample pellets, 100 mg of potassium bromide (KBr) and 1 mg of crushed sample were thoroughly mixed. The PerkinElmer Frontier Spectrophotometer was then used to collect the FTIR spectra range of 400 to 4000 cm^{-1}.

The micromorphology of selected mixes was studied using an Apreo LoVac model FE-SEM at the magnification level of 10,000×. Firstly, samples were oven dried for 24 h at 50 °C. Prior to SEM imaging, samples were coated with a gold coating for a duration of 30 s using a Leica Ultra Microtome EM UC7 sputter coater with a 20-mA current.

Results and discussion

Table 6 displays the S/N ratio for the initial setting time, final setting time, flowability, and f'$_{cu}$. The mean S/N ratio $(S/N)_{mean}$ is then computed using this S/N ratio to determine the best mix for each property. High (S/N)mean values signify the optimum level of parameters required to achieve the best results corresponding to a particular property. For example, to obtain a high initial setting time, the optimum level of parameters are 25% EAFS, 0.45 A/B, 12 SH molarity, and 2.5 SS/SH.

Consistency

Setting time

The initial and final setting time of EFGP mixes (M1–M16) range from 25 to 320 min, and 300 to 910 min, respectively

Table 6 S/N ratio of EFGP properties based on the Taguchi method

Mix no	(S/N) ratio			
	IST	FST	FV	f'_{cu}
M1	27.9	49.5	32	13.2
M2	31.6	50.7	34.8	22.1
M3	38.6	52.5	36.3	27.4
M4	33.9	52.2	36.9	26.4
M5	39.5	53.8	34.8	27.9
M6	40.4	54.6	36.9	26.4
M7	41.5	55	39.5	31.2
M8	42.2	55.8	40.8	30.8
M9	40.4	56.7	34.8	25.3
M10	40.8	57	39.4	29.3
M11	45.5	57.3	40.9	32.1
M12	46	57.6	42.1	24.8
M13	44.3	58.1	36.2	22.8
M14	46.4	58.4	39.5	25.8
M15	49.2	58.6	41.2	28.6
M16	50.1	59.1	42.6	20.2

IST initial setting time, *FST* final setting time, *FV* flowability

(Table 5). Figure 5 shows the $(S/N)_{mean}$ for setting times for the four parameters (EAFS, A/B, SH molarity, SS/SH).

The $(S/N)_{mean}$ for initial and final setting time for 25% EAFS is ~ (48 and 59), respectively. This ratio noticeably reduces to ~ (33 and 51) for 100% EAFS. Due to the reactive calcium ions present in EAFS, the speed of the geopolymeric reaction increases to produce calcium aluminosilicate hydrate gel, which attributes to a shorter setting time (Hadi et al. 2017). Further, it is also observed in Fig. 5 that a lower A/B ratio, in general, results in a lower $(S/N)_{mean}$ for the setting times. A lower A/B ratio results in a quicker setting since the overall liquid content is less. Previous studies have shown that lowering the A/B ratio would make the mix less cohesive, and speed up the geopolymerization reaction (Rafeet et al. 2017), (Rao et al. 2015). A slight decline in $(S/N)_{mean}$ for initial setting time from 43.7 to 43.1 when A/B reaches to 0.5 from 0.45 is observed. This variation is not much significant and could be attributed to other factors such as EAFS content. According to Fig. 5, neither SH molarity nor SS/SH significantly affect the setting time. Longer setting times were observed when the molarity and SS/SH were increased from 8 to 12 M and 1.5 to 2.5, respectively. This behavior is explained by the fact that at a lower molarity and SS/SH ratio, Ca^{2+} ions are readily available and react with the alkaline solution to form C-A-S–H gel, whereas at a

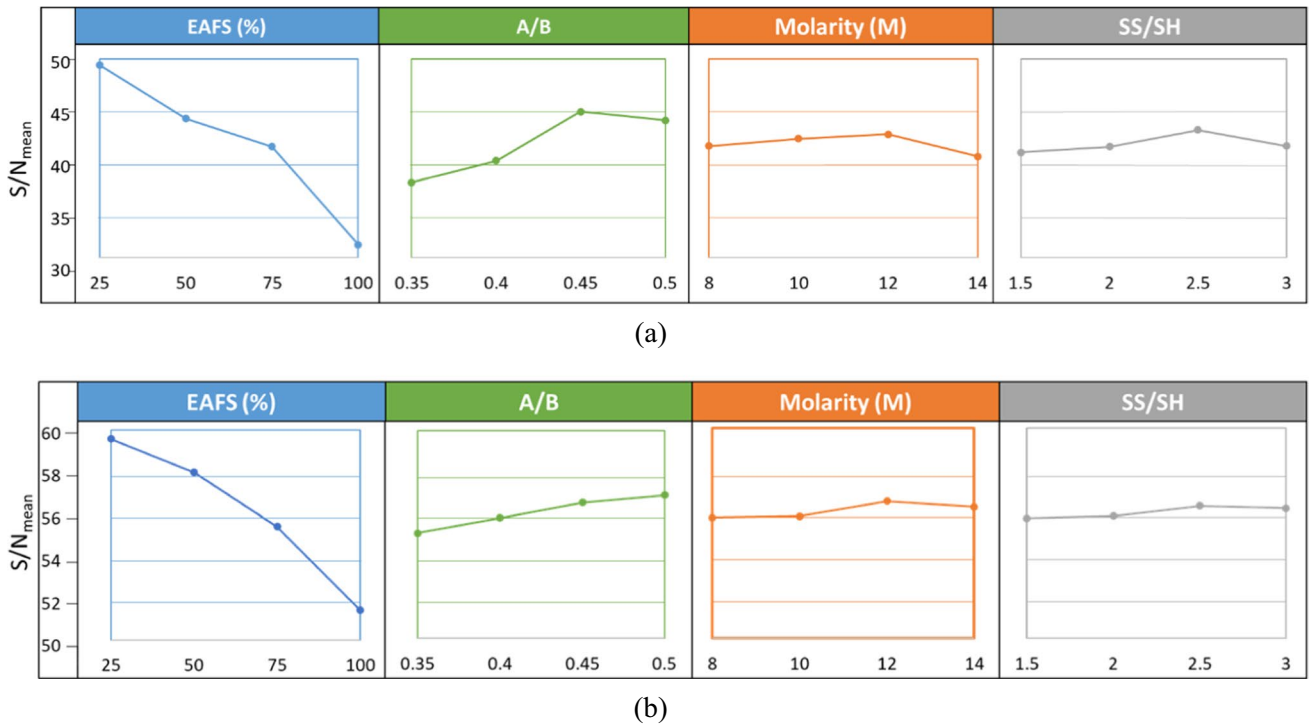

Fig. 5 $(S/N)_{mean}$ for **a** initial setting time and **b** final setting time of EFGP owing to the effects of parameters

higher molarity and SS/SH ratio, Na^+ and OH^- ions are more abundant in the matrix and also Si/Al species dissolve more slowly than Ca^{2+} ions, resulting in a higher setting time. This pattern is also consistent with earlier studies (Malkawi et al. 2016), (Rifaai et al. 2019). However, a contrary trend was seen when the molarity and SS/SH were raised from 12 to 14 M and 2.5 to 3.0. Increasing the molarity and SS/SH increases the amount of soluble silica and the dissolution of Al and Si species in the system increases the speed of the geopolymerization reaction (Elyamany et al. 2018), (Nath and Sarker 2014).

Flowability

The variation in flowability is dominantly affected by alkaline liquid and EAFS content. Figure 6 shows the $(S/N)_{mean}$ for flowability. Flow is observed to increase with an increase in EAFS replacement by fly ash. This is explained by the fact that calcium ions present in the EAFS hamper the flow owing to their rapid reactivity. Also, angular-shaped EAFS particles hinder inter-particle movements (Deb et al. 2014), while spherical-shaped fly ash particles improve the rheological characteristics of the fresh paste (Rashad 2013). The $(S/N)_{mean}$ for flowability with an A/B ratio 0.50 is ~ 41 and reduces to ~ 35 for A/B 0.35. A higher A/B ratio provides a greater fluid medium resulting in a larger inter-particle distance and reduced interaction among particles (Sathonsaowaphak et al. 2009). SH molarity is not found to have a significant impact on the flowability of the mixes (the $(S/N)_{mean}$ for SH 8 to 14 M ranged only from 37.8 to 38.2). However, during the experiment, it was found that higher molarity makes the activator solution more viscous as also noted by Memon et al. (Memon et al. 2013). A decrease was noted in $(S/N)_{mean}$ from 38.3 to 37.4 with an increase in SS/SH ratio from 1.5 to 3.0 which may be due to the higher viscosity of SS than SH. A similar trend was reported by Nath et al. (Nath and Sarker 2014).

Compressive strength

The compressive strength of the EFGP (M1-M16) mix is shown in Fig. 7. Among all the mixes, M1 exhibited the lowest compressive strength of 4.6 MPa whereas M11 showed high strength of 40.4 MPa, respectively. This variation in strength has been discussed herein through the $(S/N)_{mean}$ of the parameters (Fig. 8).

The mixes M1 to M4 (100% EAFS) are found to have the lowest $(S/N)_{mean}$ of ~ 22 due to inadequate reactive silica resulting in an insufficient amount of calcium alumino-silicate gel C-A-S–H gels formation (Ozturk et al. 2019). The $(S/N)_{mean}$ increased to ~ 29 with 25% EAFS replacement. This is due to the high calcium oxide content in EAFS which leads to the development of C-A-S–H gel, while the rich silica and alumina content in fly ash aids the formation of sodium alumino-silicate (N-A-S–H) gel (Rashad et al. 2021). The co-existence of the C-A-S–H and N-A-S–H gel attributes to the improved strength and substantially reduces the microvoids and compacts the matrix (Palomo et al. 2007) (Rashad 2014). Further, a subsequent replacement of EAFS slows the pace of gaining strength as observed from the $(S/N)_{mean}$ values which decline to ~ 24 at 75% EAFS replacement. This is due to a higher percentage of fly ash in the mix, which requires heat curing for N-A-S–H gel development (Noushini and Castel 2016). The $(S/N)_{mean}$ enhances from ~ 22 to 30 as the A/B ratio increases from 0.35 to 0.45, thereafter a decline is noticed to ~ 26, for the A/B ratio 0.50. The adequate activator content supports the dissolution of SiO_2 from the precursor to produce geopolymeric gels, improving the compressive strength (Yaseri et al. 2017). Further rise in the A/B ratio to 0.5 leads to a reduction in compressive strength due to the abundant liquid content. However, the geopolymerization process was left incomplete when the A/B ratio was 0.35, which led to the minimum compressive strength (Shoaei et al. 2019). The compressive strength gradually increases by increasing the SH molarity from 8 to 14 with $(S/N)_{mean}$ increasing from ~ 23 to 27.

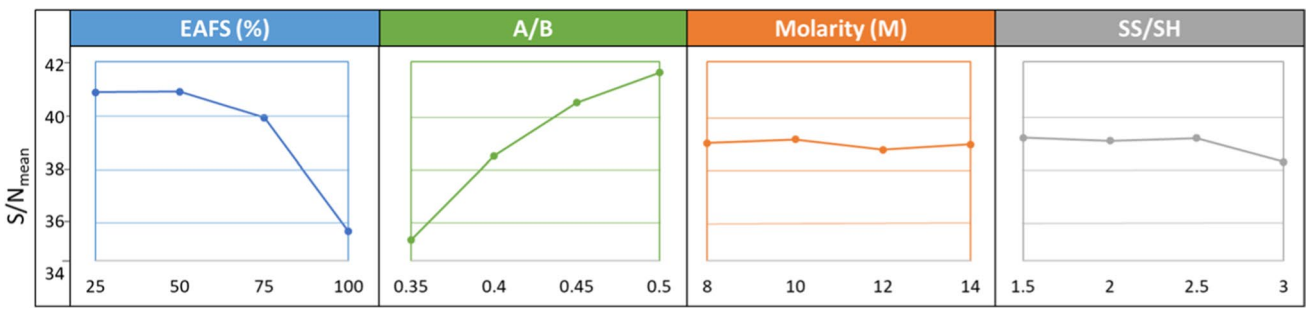

Fig. 6 $(S/N)_{mean}$ for flowability of EFGP owing to the effects of parameters

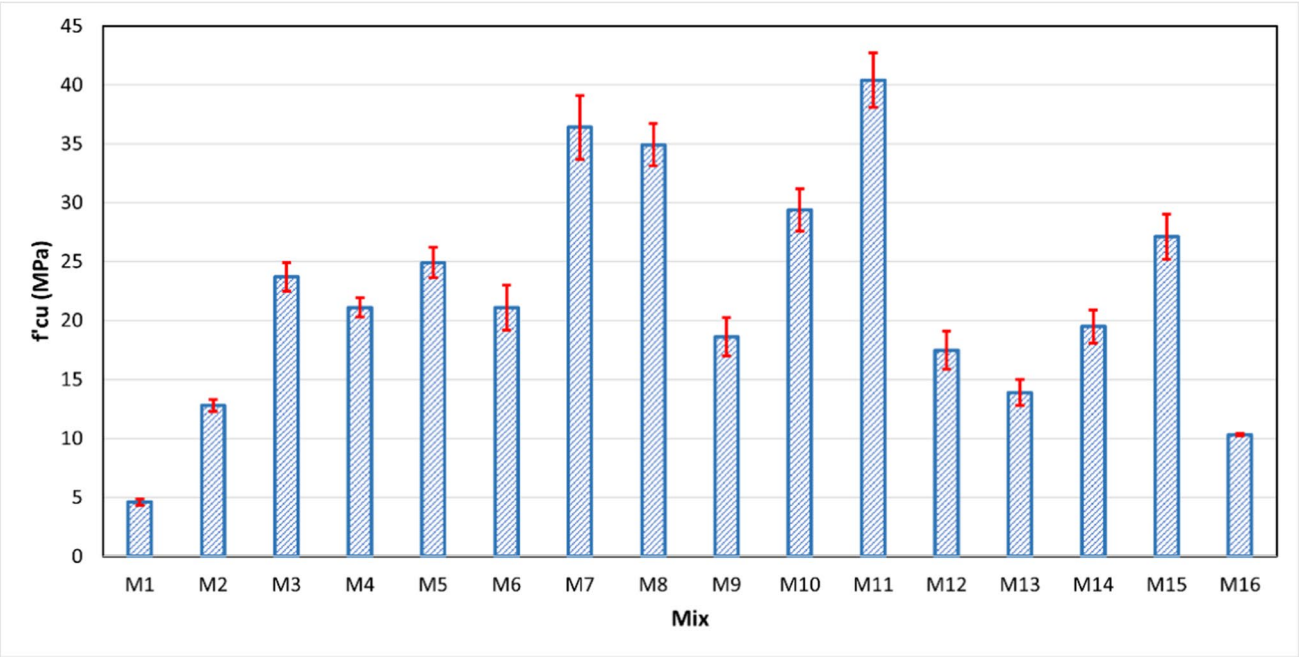

Fig. 7 The 28-day compressive strengths of EFGP mixes

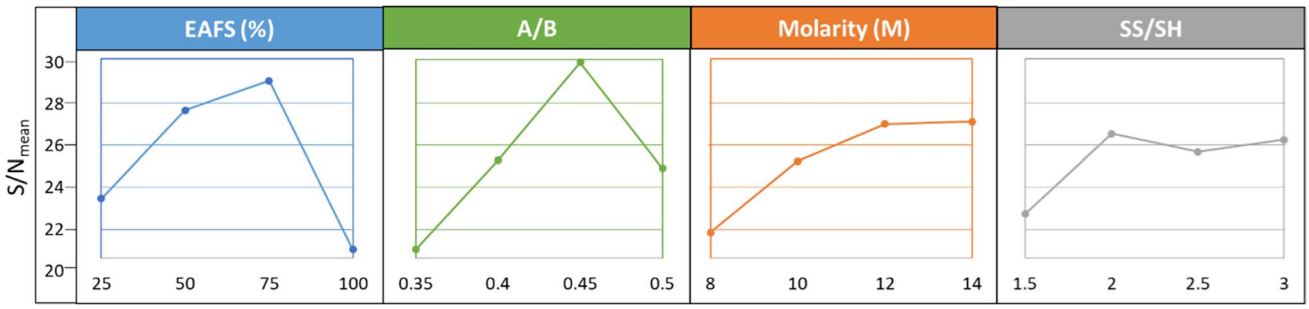

Fig. 8 $(S/N)_{mean}$ for f'_{cu} of EFGP owing to the effects of parameters

This upward trend is due to a higher dissolution of Si^{4+} and Al^{3+} from the precursor (Chindaprasirt et al. 2009). A high molarity of SH is responsible for the greater dissolution of Si^{4+} and the formation of Si–O-Si bonds, which are comparatively more stable and stronger than Al–O–Si bonds (Faradilla et al. 2020). Additionally, the $(S/N)_{mean}$ increases with an increasing SS/SH ratio. The presence of soluble silicates supports the geopolymeric reaction and contributes to strength gain (Gao et al. 2014). However, too high silicate content inhibited the geopolymerization (Bignozzi et al. 2014). The Si and Al ions from the EAFS particles are less likely to leach out when the concentration of SH is reduced which tends to enhance the viscosity of the mix. Other alkali-activated materials exhibited a similar pattern (Sukmak et al. 2013; Bignozzi et al. 2014).

Table 7 Contribution of parameters (in%) towards EFGP properties

Properties	EAFS	A/B	SH	SS/SH
IST	79.7	15.8	1.3	1.3
FST	78.4	2.2	13.7	3.3
FV	38.9	59.2	0.2	1.4
f'_{cu}	35.1	33.9	15.4	7.8

IST initial setting time, *FST* final setting time, *FV* flowability

Parametric contribution

Table 7 shows the ANOVA results for the percentage contribution of the four parameters toward setting time, flowability, and compressive strength. EAFS content has the most significant effect on tailoring

Table 8 Best mix proportions for EFGP properties

Properties	EAFS (%)	A/B	Molarity (M)	SS/SH
M_{IST}	25	0.45	12	2.5
M_{FST}	75	0.5	12	2
M_{FV}	25	0.5	10	1.5
$M_{28\ days\text{-}f'cu}$	75	0.45	14	2

IST initial setting time, *FST* final setting time, *FV* flowability

initial and final setting time, and $f'_{cu;}$ while the A/B ratio more dominantly controls the flowability of the geopolymer mix. It is also evident from the results that SS/SH ratio has very less effect on the EFGP properties.

Grey relational analysis (GRA): optimization of process parameters

Table 8 lists the best-performing parameters for EFGP in terms of initial and final setting time, flowability, and compressive strength. These values correlate to the largest $(S/N)_{mean}$. The "highest is the best" function is used for calculating the S/N ratio for IST, FV, and f'_{cu}. Moreover, to optimize the final setting time of EFGP to that of OPC, i.e., 600 min (British Standards Institution BSI 2016) and to eliminate the detrimental effect of the S/N ratio which was calculated by the "lowest is the best" function to reach the optimum mix, Eq. 6 was employed.

$$FST_i = \mathrm{abs}\left(600 - f_i(\mathrm{k})\right); i = 1 \text{ to } 16 \tag{6}$$

where FST_i is the final setting time after optimizing, $f_i(k)$ is the actual final setting time obtained through experimentation.

The S/N for FST(O) is obtained from Eq. 2 and the $(S/N)_{mean}$ is then calculated and displayed in Fig. 9.

In the current work, the best mix was determined using the GRA technique considering all the parameters. Table 9 displays the computed values for these parameters for L_{16} orthogonal mixes. The mix M8 had the third-highest compressive strength (Table 5) and the highest grey relational grade (GRG) 0.80 (Table 9) when proportioned with EAFS 75%, A/B 0.5, SH 12 M, and SS/SH 2. It might not be the optimum mix, despite having a sufficient initial setting time 130 min, final setting time 620 min, flowability 110%, and compressive strength (34.9 MPa). The GRG was calculated by the grey relational coefficient (GRC) for all parameters. The level with the highest GRG out of all the parameter levels is the best since it will have the maximum effect on the results (Kuo et al. 2008).

Furthermore, to obtain the optimum mix, Taguchi was then applied to the GRG (Table 9) for L_{16} orthogonal mixes. As a result, displayed in Fig. 10 the predicted optimum level obtained from the highest $(S/N)_{mean}$ are EAFS 75%, A/B 0.45, SH molarity 12 M, and SS/SH ratio 2.

Performance of the optimal mix: a validation

The optimized EFGP mix (designated as M17) obtained from Fig. 9 was experimentally investigated and the results are stated in Table 10. The M17, i.e., optimized EFGP mix exhibited satisfactory initial and final setting time of 127 and 581 min, flowability of 108%, and f'_{cu} 38.9 MPa, when compared with M1 to M16. The optimal EFGP mix (M17) has a GRG of 0.82, which is the highest among all other mixes (Tables 9 and 10). This shows that when initial and final setting time, flowability and f'_{cu} were all considered, the M17 mix outperformed all other mixes. The optimized mix M17 and the mix M8 (which obtained rank 1 via GRA), underwent durability testing (water absorption test) and microstructural examinations using XRD, FTIR, and SEM.

Water absorption is one of the factors determining the durability of the mix. A higher water absorption signifies greater porosity, which leads to strength degradation in long term. Water absorption decreases with the addition of fly ash due to the development of geopolymeric gel and also due to fly ash acting as a micro filler (Somna et al. 2011; He et al. 2013). The water absorption for M8 and M17 mixes are 12.2% and 10.95%, respectively. A sufficiently low water

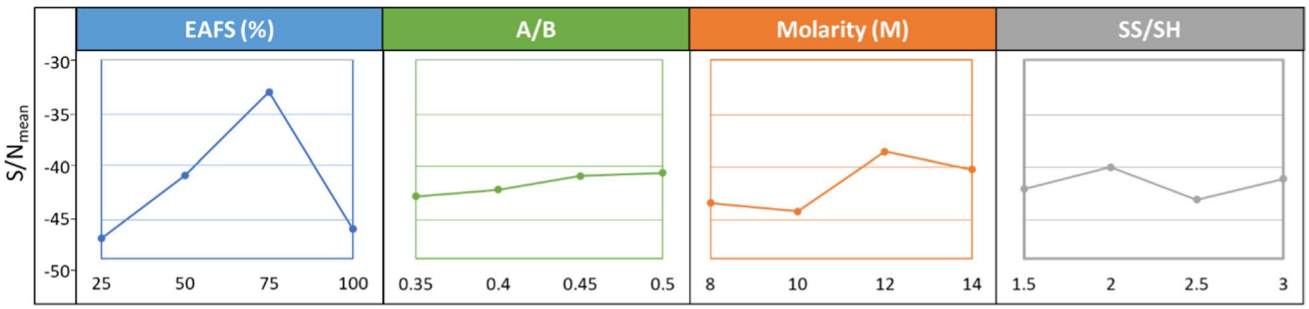

Fig. 9 $(S/N)_{mean}$ of the optimized final setting time of EFGP due to parameters

Table 9 GRG of each EFGP mix through the GRA technique

Mix	Normalized S/N ratio				Deviation sequence				GRC				GRG	Rank
	IST	FST	FV	f'_{cu}	IST	FST	FV	f'_{cu}	IST	FST	FV	f'_{cu}		
M1	0	0.01	0	0	1	0.99	1	1	0.33	0.34	0.33	0.33	0.33	16
M2	0.16	0.07	0.26	0.47	0.84	0.93	0.74	0.53	0.37	0.35	0.4	0.49	0.4	15
M3	0.48	0.21	0.41	0.75	0.52	0.79	0.59	0.25	0.49	0.39	0.46	0.67	0.5	11
M4	0.27	0.18	0.46	0.7	0.73	0.82	0.54	0.3	0.41	0.38	0.48	0.63	0.47	14
M5	0.52	0.39	0.26	0.78	0.48	0.61	0.74	0.22	0.51	0.45	0.4	0.69	0.52	10
M6	0.56	0.6	0.46	0.7	0.44	0.4	0.54	0.3	0.53	0.56	0.48	0.63	0.55	9
M7	0.62	0.8	0.71	0.95	0.38	0.2	0.29	0.05	0.57	0.71	0.63	0.91	0.71	3
M8	0.65	1	0.83	0.93	0.35	0	0.17	0.07	0.59	1	0.75	0.88	0.8	1
M9	0.56	0.47	0.26	0.64	0.44	0.53	0.74	0.36	0.53	0.49	0.4	0.58	0.5	12
M10	0.58	0.36	0.7	0.85	0.42	0.64	0.3	0.15	0.54	0.44	0.63	0.77	0.6	7
M11	0.8	0.3	0.85	1	0.2	0.7	0.15	0	0.71	0.42	0.77	1	0.72	2
M12	0.82	0.24	0.96	0.61	0.18	0.76	0.04	0.39	0.73	0.4	0.92	0.56	0.65	6
M13	0.74	0.14	0.4	0.51	0.26	0.86	0.6	0.49	0.66	0.37	0.45	0.5	0.5	13
M14	0.83	0.1	0.71	0.66	0.17	0.9	0.29	0.34	0.75	0.36	0.63	0.6	0.59	8
M15	0.96	0.06	0.88	0.82	0.04	0.94	0.12	0.18	0.93	0.35	0.8	0.73	0.7	4
M16	1	0	1	0.37	0	1	0	0.63	1	0.33	1	0.44	0.69	5

IST initial setting time, *FST* final setting time, *FV* flowability, *GRC* grey relational coefficient, *GRG* grey relational grade

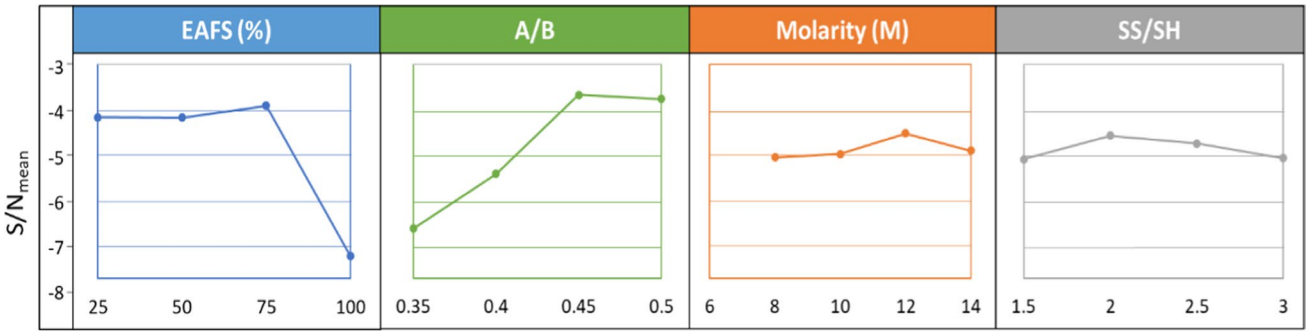

Fig. 10 $(S/N)_{mean}$ for GRG with respect to the optimum mix

Table 10 Performance of M17 mix (EAFS = 75%, A/B = 0.45, SH = 12 M, and SS/SH = 2)

Property	Output	S/N ratio	GRG
IST (min)	127	42	0.82
FST (min)	582	−33.2	
FV (%)	108	40.6	
f'_{cu} (MPa)	38.9	31.7	

IST initial setting time, *FST* final setting time, *FV* flowability

absorption in both mixes is due to an adequate geopolymerization reaction which aids in stabilizing the matrix and effectively reducing the porosity (Yong-Sing et al. 2022).

Figure 11 displays the XRD patterns of the precursors fly ash, EAFS, M8 geopolymer, and M17 geopolymer. The crystalline phases of quartz, mullite, hematite, gehlenite, and merwinite were prominently visible in precursors and M8 geopolymer and M17 geopolymer (Hui-Teng et al. 2021; Rashad et al. 2021), as their dissolution in the alkaline medium is difficult (Xing et al. 2019). However, the depiction of calcite in EAFS and its presence in M8 and M17 geopolymer with reduced intensity was recorded after the addition of fly ash. Similar results were reported by (Rashad et al. 2021). Moreover, It is hypothesized that calcium linked with calcite reacts with silicate and forms geopolymeric gel. This is in addition to the fact that there are no new traces of crystalline phases in M17 and M8 (Yip et al. 2008). The formation of geopolymeric gel was also confirmed as a broad amorphous halo was observed at (23°–32°) 2θ.

The SEM images of the M8 and M17 mix are presented in Fig. 12. The presence of geopolymeric gel is noticed in both

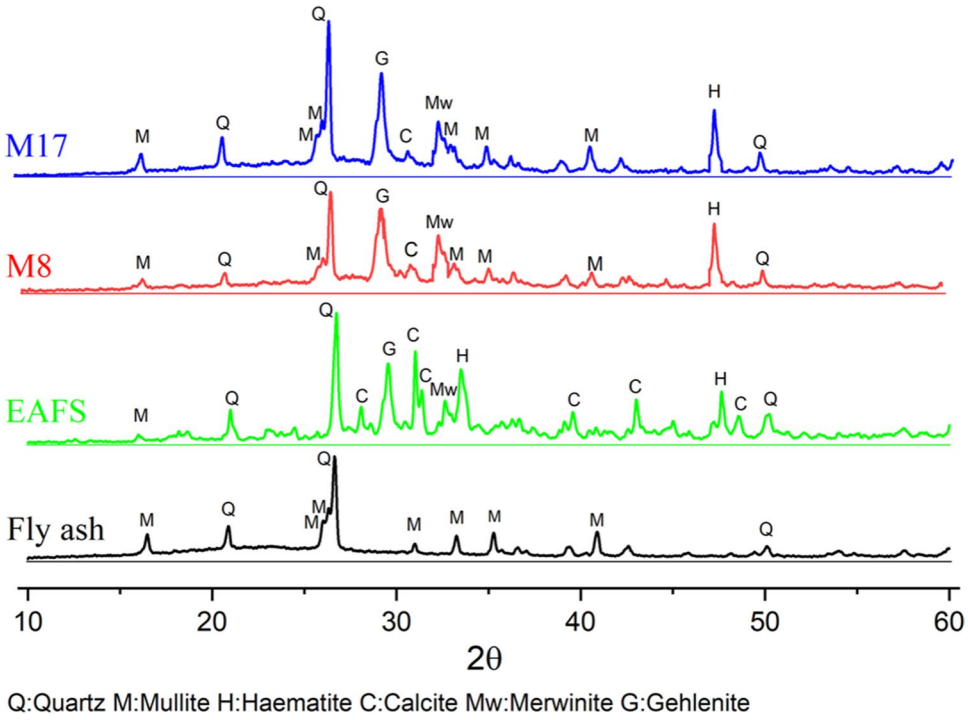

Fig. 11 XRD pattern of Fly ash, EAFS, M8, and M17 mix

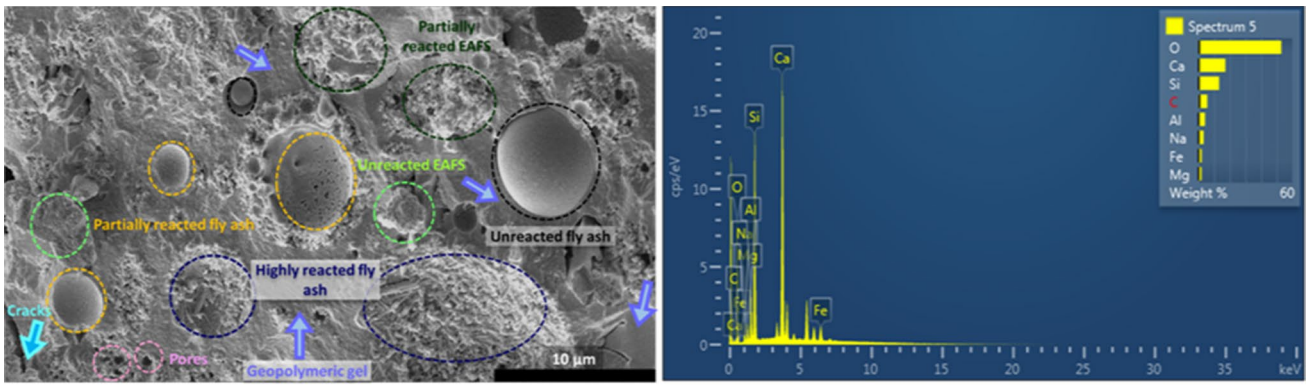

(a)

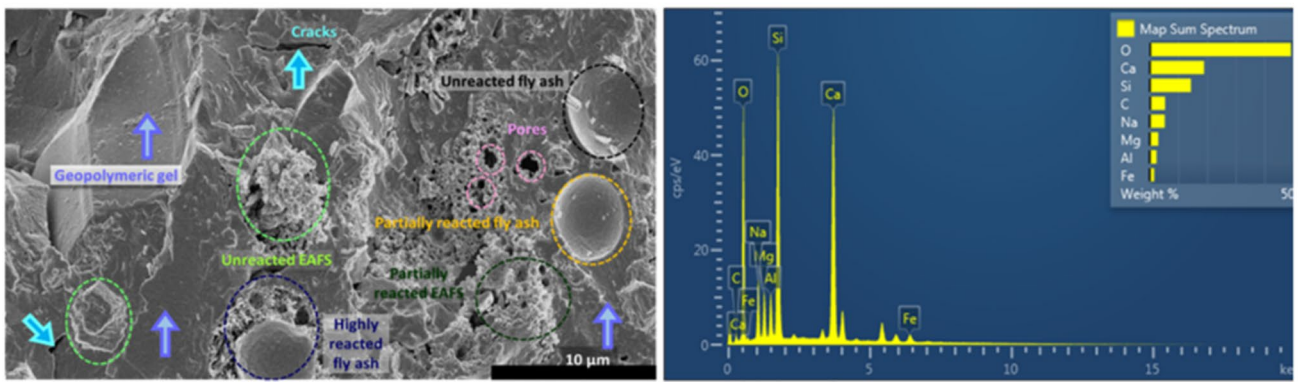

(b)

Fig. 12 SEM images showing the microstructure of **a** Mix M8; **b** Mix M17

mixes confirming the good strength development of both mixes. A dense microstructure along with some micropores, micro-cracks, and regions of partial geopolymerization are observed in both mixes. Besides, spherical fly ash particles with crystalline portions (rod-shaped morphology) could be observed in the SEM images. This indicates that the amorphous portion of fly ash could participate in the N-A-S–H gel formation while the crystalline portion remained largely unaffected as supported by the previous work (Ambikakumari Sanalkumar et al. 2019). Furthermore, heat curing, in contrast to ambient curing (purposefully chosen in this study), might lead to a higher degree of geopolymerization

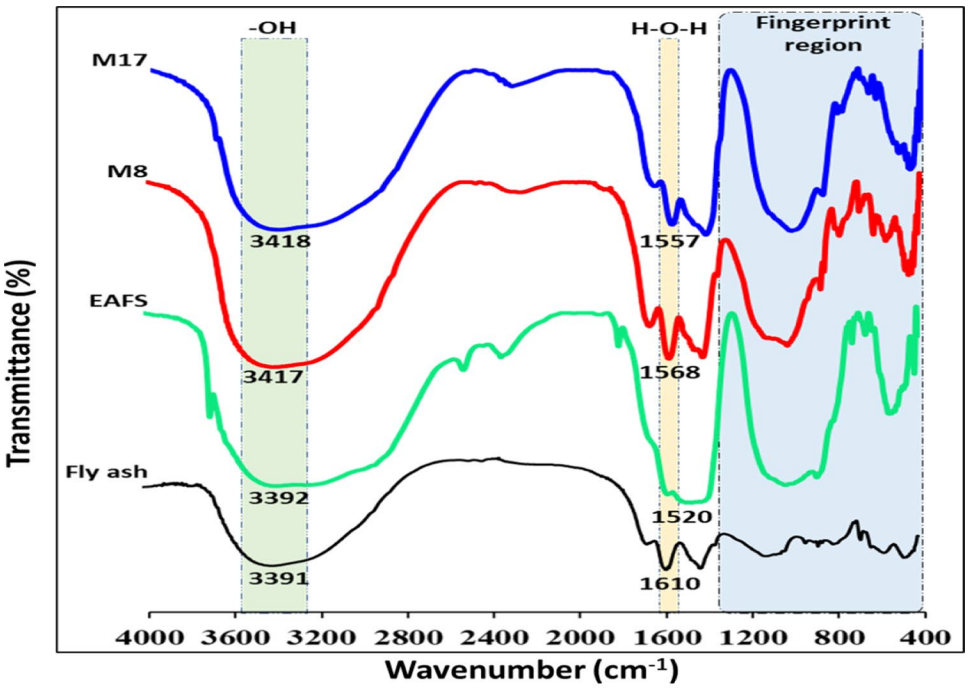

(a)

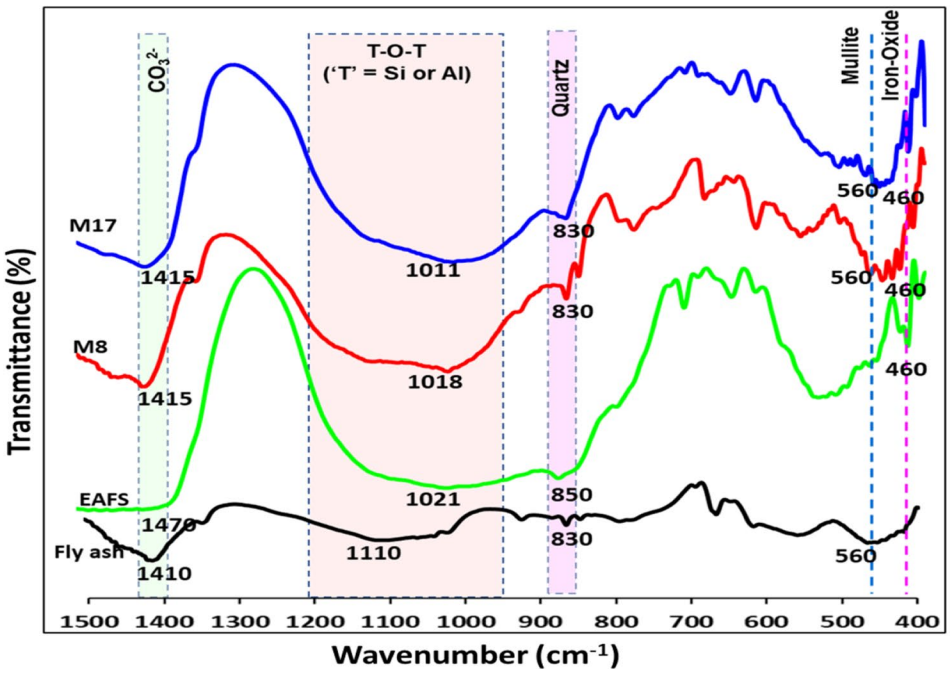

(b)

Fig. 13 FTIR patterns of fly ash, EAFS, M8, and M17 mixes **a** 4000 cm^{-1} to 400 cm^{-1}. **b** Fingerprint region: 1500 cm^{-1} to 400 cm^{-1}.[1]

and lesser amounts of unreacted and partially reacted EAFS and fly ash, and better strength development (Singh et al. 2015). The micro-cracks and micropores observed are responsible for water absorption. These results corroborate well with the literature (Ozturk et al. 2019; Nikolic et al. 2020; Rashad et al. 2021).

FTIR analysis was used to examine the functional groups and bonds present in the precursors as well as in M8 and M17 geopolymer mixes. Figure 13 displays FTIR spectrums of raw fly ash, EAFS, and M8 and M17 geopolymer mixes. It was noted that the main asymmetric stretching band of the T-O-T (where 'T' is silicon or aluminum) bonds for fly ash was centered at 1110 cm^{-1}, and for EAFS at 1021 cm^{-1}. The mix M8 shows a shift in the T-O-T peak to 1018 cm^{-1} and in M17 mix the peak gets shifted to 1011 cm^{-1}. This shift of peak corresponding to T-O-T bonds to a longer wavelength is the result of the alkaline activation of the precursors (Hui-Teng et al. 2021). These results align with the SEM observation that the microstructure of M8 and M17 mixes is largely homogenous (with some micropores, micro-cracks, and regions of partial geopolymerization) owing to a good degree of alkali activation, thereby leading to considerable compressive strengths in these mixes. Besides, the broad peak ascribed to the stretching of OH group is observed at 3391 cm^{-1}, 3392 cm^{-1}, 3417 cm^{-1} and 3418 cm^{-1} for fly ash, EAFS, M8 and M17, respectively. The presence of H–O-H was also discovered at 1610 cm^{-1}, 1520 cm^{-1}, 1568 cm^{-1}, and 1557 cm^{-1} for fly ash, M8, and M17. The notable peaks at 1410 cm^{-1}, 1470 cm^{-1}, 1415 cm^{-1}, and 1415 cm^{-1} for fly ash, EAFS, M8, and M17 were attributable to the deformation vibration of the CO_3^{2-} group (Khater 2015) indicating the presence of calcite in the system. The peaks corresponding to quartz and mullite, could be observed at 830 cm^{-1} and 560 cm^{-1}, respectively. The spectrum of EAFS, M8, and M17 also detected the presence of iron oxides at 460 cm^{-1} (Sosa et al. 2021) due to the presence of hematite which was also observed through XRD.

Conclusions

This study investigated the synergistic effect of parameters, namely, EAFS replacement level, alkaline solution to binder (A/B) ratio, SH molarity, and SS/SH ratio on the compressive strength, setting times, and flowability of ambient cured EAF slag-fly ash based geopolymer (EFGP). The use of the Taguchi method of design of experiments saved time, effort, and cost by reducing the number of experiments to merely 16. Furthermore, grey relational analysis (GRA) effectively determined the optimal set of parameters for the development of EFGP. It was noted that the EAFS replacement ratio and the A/B ratio were the most significant factors for tailoring the properties of ambient-cured EFGP. Besides, the optimal composition was found to be 75% EAFS, A/B = 0.45, SH = 12 M, and SS/SH = 2, and the corresponding geopolymer mix was labeled as M17. The validation experiment results on the M17 mix confirmed the GRA results. This mix produced the highest compressive strength ~ 39 MPa accrediting to the development of (C, N)-A-S–H gel (as observed through the SEM micrographs, and also corroborated by XRD and FTIR results). The initial and final setting times of this mix were also optimized at 127 min and 581 min, respectively, owing to adequate alkali and amorphous contents in the matrix. The flowability was 108% due to sufficient activator content as well as the spherical shape of fly ash particles. A sufficiently low water absorption (10.95%) was also noted in this mix. The results indicate that sustainable development of EAF slag and fly ash geopolymer could be achieved using Taguchi-GRA optimization.

Authors' contributions Anant Mishra: conceptualization, methodology, investigation, software, writing—original draft. Mukund Lahoti: investigation, supervision, writing, review, and editing. En-Hua Yang: supervision, review, and editing. All authors read and approved the final manuscript.

Funding The authors would like to thank Birla Institute of Technology and Science Pilani, Pilani Campus, India, for its help in providing the necessary funding and facilities needed to perform this research.

Data availability Data will be made available on request.

Declarations

Ethics approval and consent to participate Not applicable.

Consent to participate Not applicable.

Consent for publication Not applicable.

Competing interests The authors declare that they have no competing interests.

References

Aayog NITI, Action EE (2018) Strategy paper on resource efficiency in steel sector through recycling of scrap & slag. Ministry of Steel, Government of India. https://www.srtmi.com/uploads/pdf/RE_Steel_Scrap_Slag-NITIayog-28092018.pdf

AmbikakumariSanalkumar KU, Lahoti M, Yang EH (2019) Investigating the potential reactivity of fly ash for geopolymerization. Constr Build Mater 225:283–291. https://doi.org/10.1016/j.conbuildmat.2019.07.140

Apithanyasai S, Supakata N, Papong S (2020) The potential of industrial waste: using foundry sand with fly ash and electric arc furnace slag for geopolymer brick production. Heliyon 6:e03697. https://doi.org/10.1016/j.heliyon.2020.e03697

Arslanoglu N (2017) Investigation of efficient parameters on optimum insulation thickness based on theoretical-Taguchi combined

method. Wiley Online Libr 36:1824–1831https://doi.org/10.1002/ep.12628
Assi LN, Carter K, Deaver E, Ziehl P (2020) Review of availability of source materials for geopolymer/sustainable concrete. J Clean Prod 263:121477. https://doi.org/10.1016/j.jclepro.2020.121477
ASTM C191 (2013) Standard test methods for time of setting of hydraulic cement by vicat needle. ASTM International, West Conshohocken, PA
ASTM C 618 (2014) Standard specification for coal fly ash and raw or calcined natural pozzolan for use in concrete, ASTM International, West Conshohocken, PA, 2012, www.astm.org.ASTM Int 1–5. https://doi.org/10.1520/C0618
ASTM C109 (2008) Standard test method for compressive strength of hydraulic cement mortars (using 2-in. or [50-mm] cube specimens), pp 1–9. https://www.astm.org/c0109_c0109m-20.html
Astm (2001) Standard test method for flow of hydraulic cement mortar: C1437–01. Standard 7–8. https://doi.org/10.1520/C1437-20.2
Bajpai R, Choudhary K, Srivastava A et al (2020) Environmental impact assessment of fly ash and silica fume based geopolymer concrete. J Clean Prod. https://doi.org/10.1016/j.jclepro.2020.120147
Bignozzi MC, Barbieri L, Lancellotti I (2010) New geopolymers based on electric arc furnace slag. Adv Sci Technol 69:117–122. https://doi.org/10.4028/www.scientific.net/ast.69.117
Bignozzi MC, Manzi S, Natali ME et al (2014) Room temperature alkali activation of fly ash: the effect of Na 2O/SiO2 ratio. Constr Build Mater 69:262–270. https://doi.org/10.1016/j.conbuildmat.2014.07.062
British Standards Institution (BSI) (2016) BS EN 196-3:2016: Methods oftesting cement, part 3: Determination of Setting Time and Soundness. BSI, London. https://www.en-standard.eu/bs-en-196-3-2016-methods-of-testing-cement-determination-of-setting-times-and-soundness/
Češnovar M, Traven K, Horvat B, Ducman V (2019) The potential of ladle slag and electric arc furnace slag use in Synthesizing alkali activated materials; the influence of curing on mechanical properties. Materials (Basel) 12. https://doi.org/10.3390/ma12071173
Chindaprasirt P, Jaturapitakkul C, Chalee W, Rattanasak U (2009) Comparative study on the characteristics of fly ash and bottom ash geopolymers. Waste Manag 29:539–543. https://doi.org/10.1016/j.wasman.2008.06.023
Cristelo N, Coelho J, Miranda T et al (2019) Alkali activated composites – an innovative concept using iron and steel slag as both precursor and aggregate. Cem Concr Compos 103:11–21
Davidovits J (1989) Geopolymers and geopolymeric materials. J Therm Anal 35:429–441. https://doi.org/10.1007/BF01904446
Deb PS, Nath P, Sarker PK (2014) The effects of ground granulated blast-furnace slag blending with fly ash and activator content on the workability and strength properties of geopolymer concrete cured at ambient temperature. Mater Des 62:32–39. https://doi.org/10.1016/j.matdes.2014.05.001
Duxson P, Fernández-Jiménez A, Provis JL et al (2007) Geopolymer technology: the current state of the art. J Mater Sci 42:2917–2933. https://doi.org/10.1007/s10853-006-0637-z
Elyamany HE, AbdElmoaty AEM, Elshaboury AM (2018) Setting time and 7-day strength of geopolymer mortar with various binders. Constr Build Mater 187:974–983. https://doi.org/10.1016/j.conbuildmat.2018.08.025
Faradilla FS, Nugroho DT, Hidayati RE, et al (2020) Optimization of SiO2/Al2O3 ratio in the preparation of geopolymer from high calcium fly ash. IOP Conf Ser Earth Environ Sci 616. https://doi.org/10.1088/1755-1315/616/1/012051
Gao K, Lin KL, Wang D et al (2014) Effects SiO2/Na2O molar ratio on mechanical properties and the microstructure of nano-SiO2 metakaolin-based geopolymers. Constr Build Mater 53:503–510. https://doi.org/10.1016/j.conbuildmat.2013.12.003
Hadi MNS, Farhan NA, Sheikh MN (2017) Design of geopolymer concrete with GGBFS at ambient curing condition using Taguchi method. Constr Build Mater 140:424–431. https://doi.org/10.1016/j.conbuildmat.2017.02.131
Han F, Zhang Z, Wang D, Yan P (2015) Hydration heat evolution and kinetics of blended cement containing steel slag at different temperatures. Thermochim Acta 605:43–51. https://doi.org/10.1016/j.tca.2015.02.018
He J, Jie Y, Zhang J et al (2013) Synthesis and characterization of red mud and rice husk ash-based geopolymer composites. Cem Concr Compos 37:108–118. https://doi.org/10.1016/j.cemconcomp.2012.11.010
Hui-Teng N, Cheng-Yong H, Yun-Ming L et al (2021) Formulation, mechanical properties and phase analysis of fly ash geopolymer with ladle furnace slag replacement. J Mater Res Technol 12:1212–1226. https://doi.org/10.1016/j.jmrt.2021.03.065
IEA (2021) Net Zero by 2050: A roadmap for the global energy sector. Int Energy Agency 224. https://www.iea.org/reports/net-zero-by-2050
IS : 4031 (Part 5) (2000) IS : 4031 (Part 5) - 1988 (Reaffirmed 2000). https://www.iitk.ac.in/ce/test/IS-codes/is.4031.5.1988.pdf
J TG (1987) Taguchi techniques for quality engineering. Water Air Soil Pollut 203:53–63. https://doi.org/10.1007/s11270-009-9991-1
Jamshaid H, Ahmad N, Hussain U, Mishra R (2022) Parametric optimization of durable sheeting fabric using Taguchi Grey Relational Analysis. J King Saud Univ - Sci 34. https://doi.org/10.1016/j.jksus.2022.102004
Khater HMM (2015) Influence of electric arc furnace slag on characterisation of the produced geopolymer composites. Epa - J Silic Based Compos Mater 67:82–88. https://doi.org/10.14382/epitoanyag-jsbcm.2015.13
Kuo Y, Yang T (2008) The use of a grey-based Taguchi method for optimizing multi-response simulation problems. Taylor Fr 40:517–528. https://doi.org/10.1080/03052150701857645
Lahoti M, Tan KH, Yang EH (2019) A critical review of geopolymer properties for structural fire-resistance applications. Constr Build Mater 221:514–526. https://doi.org/10.1016/j.conbuildmat.2019.06.076
Li L, Ling TC, Pan SY (2022) Environmental benefit assessment of steel slag utilization and carbonation: a systematic review. Sci Total Environ 806:150280. https://doi.org/10.1016/j.scitotenv.2021.150280
Malkawi AB, Nuruddin MF, Fauzi A et al (2016) Effects of alkaline solution on properties of the HCFA geopolymer mortars. Procedia Eng 148:710–717. https://doi.org/10.1016/j.proeng.2016.06.581
McLellan BC, Williams RP, Lay J et al (2011) Costs and carbon emissions for geopolymer pastes in comparison to ordinary portland cement. J Clean Prod 19:1080–1090. https://doi.org/10.1016/j.jclepro.2011.02.010
Memon FA, Nuruddin MF, Khan S et al (2013) Effect of sodium hydroxide concentration on fresh properties and compressive strength of self-compacting geopolymer concrete. J Eng Sci Technol 8:44–56
Meshram RB, Kumar S (2022) Comparative life cycle assessment (LCA) of geopolymer cement manufacturing with Portland cement in Indian context. Int J Environ Sci Technol 19:4791–4802. https://doi.org/10.1007/s13762-021-03336-9
Narong OLC, Sia CK, Yee SK et al (2018) Optimisation of EMI shielding effectiveness: Mechanical and physical performance of mortar containing POFA for plaster work using Taguchi Grey method. Constr Build Mater 176:509–518. https://doi.org/10.1016/j.conbuildmat.2018.05.025
Nath P, Sarker PK (2014) Effect of GGBFS on setting, workability and early strength properties of fly ash geopolymer concrete cured in ambient condition. Constr Build Mater 66:163–171. https://doi.org/10.1016/j.conbuildmat.2014.05.080

Nazari A, Sanjayan JG (2015) Hybrid effects of alumina and silica nanoparticles on water absorption of geopolymers: Application of Taguchi approach. Meas J Int Meas Confed 60:240–246. https://doi.org/10.1016/j.measurement.2014.10.004

Nemaleu JGD, Belela EA, Nana A et al (2022) Feasibilty of valorizing quarry wastes in the synthesis of geopolymer binders: engineering performances and microstructure. Environ Sci Pollut Res 29:50804–50818. https://doi.org/10.1007/s11356-022-19415-4

Nguyen LH, Nguyen TD, Tran TVN et al (2022) Steel slag quality control for road construction aggregates and its environmental impact: case study of Vietnamese steel industry—leaching of heavy metals from steel-making slag. Environ Sci Pollut Res 29:41983–41991. https://doi.org/10.1007/s11356-021-16438-1

Niklioć I, Marković S, Janković - Častvan I et al (2016) Modification of mechanical and thermal properties of fly ash-based geopolymer by the incorporation of steel slag. Mater Lett 176:301–305. https://doi.org/10.1016/j.matlet.2016.04.121

Nikolic I, Crossed D, Signurovic D, Markovic S et al (2020) Alkali activated slag cement doped with Zn-rich electric arc furnace dust. J Mater Res Technol 9:12783–12794. https://doi.org/10.1016/j.jmrt.2020.09.024

Noushini A, Castel A (2016) The effect of heat-curing on transport properties of low-calcium fly ash-based geopolymer concrete. Constr Build Mater 112:464–477. https://doi.org/10.1016/j.conbuildmat.2016.02.210

Ozturk M, Bankir MB, Bolukbasi OS, Sevim UK (2019) Alkali activation of electric arc furnace slag: Mechanical properties and micro analyzes. J Build Eng 21:97–105. https://doi.org/10.1016/j.jobe.2018.10.005

Palomo A, Fernández-Jiménez A, Kovalchuk G et al (2007) Opc-fly ash cementitious systems: Study of gel binders produced during alkaline hydration. J Mater Sci 42:2958–2966. https://doi.org/10.1007/s10853-006-0585-7

Pellegrino C, Gaddo V (2009) Mechanical and durability characteristics of concrete containing EAF slag as aggregate. Cem Concr Compos 31:663–671. https://doi.org/10.1016/j.cemconcomp.2009.05.006

Rafeet A, Vinai R, Soutsos M, Sha W (2017) Guidelines for mix proportioning of fly ash/GGBS based alkali activated concretes. Constr Build Mater 147:130–142. https://doi.org/10.1016/j.conbuildmat.2017.04.036

Rahou J, Rezqi H, El Ouahabi M, Fagel N (2022) Characterization of Moroccan steel slag waste: the potential green resource for ceramic production. Constr Build Mater 314:125663. https://doi.org/10.1016/j.conbuildmat.2021.125663

Rao GM (2015) Final setting time and compressive strength of fly ash and GGBS-based geopolymer paste and mortar. Springer 40:3067–3074https://doi.org/10.1007/s13369-015-1757-z

Rashad AM (2013) Properties of Alkali-Activated Fly Ash. Concrete 10:57–64

Rashad AM (2014) A comprehensive overview about the influence of different admixtures and additives on the properties of alkali-activated fly ash. Mater Des 53:1005–1025. https://doi.org/10.1016/j.matdes.2013.07.074

Rashad AM, Gharieb M (2021) An investigation on the effect of sea sand on the properties of fly ash geopolymer mortars. Innov Infrastruct Solut 6:1–9. https://doi.org/10.1007/s41062-020-00421-9

Rashad AM, Khafaga SA, Gharieb M (2021) Valorization of fly ash as an additive for electric arc furnace slag geopolymer cement. Constr Build Mater 294:123570. https://doi.org/10.1016/j.conbuildmat.2021.123570

Rawat S, Zhang YX, Lee CK (2022) Multi-response optimization of hybrid fibre engineered cementitious composite using Grey-Taguchi method and utility concept. Constr Build Mater 319. https://doi.org/10.1016/j.conbuildmat.2021.126040

Rifaai Y, Yahia A, Mostafa A et al (2019) Rheology of fly ash-based geopolymer: Effect of NaOH concentration. Constr Build Mater 223:583–594. https://doi.org/10.1016/j.conbuildmat.2019.07.028

Salas DA, Ramirez AD, Rodríguez CR, et al (2016) Environmental impacts, life cycle assessment and potential improvement measures for cement production: a literature review. J Clean Prod 114–122. https://doi.org/10.1016/j.jclepro.2015.11.078

Sathonsaowaphak A, Chindaprasirt P, Pimraksa K (2009) Workability and strength of lignite bottom ash geopolymer mortar. J Hazard Mater 168:44–50. https://doi.org/10.1016/j.jhazmat.2009.01.120

Sedira N, Castro-Gomes J (2019) Effects of EAF-Slag on alkali-activation of tungsten mining waste: mechanical properties. MATEC Web Conf 274:01003. https://doi.org/10.1051/matecconf/201927401003

Shilar FA, Ganachari SV, Patil VB et al (2022) Molarity activity effect on mechanical and microstructure properties of geopolymer concrete: a review. Case Stud Constr Mater 16:e01014. https://doi.org/10.1016/j.cscm.2022.e01014

Shoaei P, Musaeei HR, Mirlohi F, et al (2019) Waste ceramic powder-based geopolymer mortars: Effect of curing temperature and alkaline solution-to-binder ratio. Constr Build Mater 227. https://doi.org/10.1016/j.conbuildmat.2019.116686

Shrivas R, Paramkusam BR, Dwivedi SB (2022) Strength and durability performance of geopolymer binder of ambient cured alkali-activated MSW rejected waste and GGBFS mixes. Environ Sci Pollut Res 29:30521–30536. https://doi.org/10.1007/s11356-021-17547-7

Singh B, Ishwarya G, Gupta M, Bhattacharyya SK (2015) Geopolymer concrete: a review of some recent developments. Constr Build Mater 85:78–90. https://doi.org/10.1016/j.conbuildmat.2015.03.036

Singh SK, Vashistha P, Chandra R, Rai AK (2021) Study on leaching of electric arc furnace (EAF) slag for its sustainable applications as construction material. Process Saf Environ Prot 148:1315–1326. https://doi.org/10.1016/j.psep.2021.01.039

Somna K, Jaturapitakkul C, Kajitvichyanukul P, Chindaprasirt P (2011) NaOH-activated ground fly ash geopolymer cured at ambient temperature. Fuel 90:2118–2124. https://doi.org/10.1016/j.fuel.2011.01.018

Sosa I, Tamayo P, Sainz-Aja JA, et al (2021) Durability aspects in self-compacting siderurgical aggregate concrete. J Build Eng 39. https://doi.org/10.1016/j.jobe.2021.102268

Steel G, Report W (2019) Green steel by EAF route : a sustainable value chain in the EU Circular Economy scenario 32:1–6. https://www.estep.eu/assets/Uploads/20191129-WorkshopReport-ESTEP-EAFGreenSteel-FinalDraft.pdf

Suji D, Adesina A, Mirdula R (2021) Optimization of self-compacting composite composition using Taguchi-Grey relational analysis. Materialia 15. https://doi.org/10.1016/j.mtla.2021.101027

Sukmak P, Horpibulsuk S, Shen SL (2013) Strength development in clay-fly ash geopolymer. Constr Build Mater 40:566–574. https://doi.org/10.1016/j.conbuildmat.2012.11.015

Thwe E, Khatiwada D, Gasparatos A (2021) Life cycle assessment of a cement plant in Naypyitaw, Myanmar. Clean Environ Syst 2:100007. https://doi.org/10.1016/j.cesys.2020.100007

World Steel Association (2011) Steel and Raw materials 15:710–739. http://www.worldsteel.org/dms/internetDocumentList/fact-sheets/Fact-sheet_Raw-materials2011/document/Factsheet_Rawmaterials2011.pdf

Worldsteel Association (2021) PRESS RELEASE – worldsteel short range outlook. https://worldsteel.org/wp-content/uploads/Press-release-worldsteel-Short-Range-Outlook-October-2021.pdf

Xing J, Zhao Y, Qiu J, Sun X (2019) Microstructural and mechanical properties of alkali activated materials from two types of blast furnace slags. Materials (Basel) 12. https://doi.org/10.3390/ma12132089

Yaseri S, Hajiaghaei G, Mohammadi F et al (2017) The role of synthesis parameters on the workability, setting and strength properties of binary binder based geopolymer paste. Constr Build Mater 157:534–545. https://doi.org/10.1016/j.conbuildmat.2017.09.102

Yip CK, Provis JL, Lukey GC, van Deventer JSJ (2008) Carbonate mineral addition to metakaolin-based geopolymers. Cem Concr Compos 30:979–985. https://doi.org/10.1016/j.cemconcomp.2008.07.004

Yong-Sing N, Yun-Ming L, Cheng-Yong H et al (2022) Thin fly ash/ladle furnace slag geopolymer: Effect of elevated temperature exposure on flexural properties and morphological characteristics. Ceram Int 48:16562–16575. https://doi.org/10.1016/j.ceramint.2022.02.201

Zaharaki D, Galetakis M, Komnitsas K (2016) Valorization of construction and demolition (C&D) and industrial wastes through alkali activation. Constr Build Mater 121:686–693. https://doi.org/10.1016/j.conbuildmat.2016.06.051

Zhang SP, Zong L (2014) Evaluation of relationship between water absorption and durability of concrete materials. Adv Mater Sci Eng 2014. https://doi.org/10.1155/2014/650373